

Regular paper

<https://doi.org/10.1631/jzus.A2200388>



Mechanistic investigation on Hg⁰ capture over MnO_x adsorbents: effects of the synthesis methods

Dong YE[✉], Yongjin HU, Zhichang JIANG, Xin LIU, Haining WANG[✉]

College of Quality & Safety Engineering, China Jiliang University, Hangzhou 310018, China

Abstract: This study demonstrated the impacts of the synthesis methods on the textural structures, chemical properties, and Hg⁰ capture capability of the MnO_x system. Compared with the samples synthesized using the precipitation (PR) and hydrothermal (HT) methods, the adsorbent prepared via the sol-gel (SG) technique gave the best performance. At 150 °C, ca. 90% Hg⁰ removal efficiency was reached after 7.5 h for MnO_x prepared by the SG method, ca. 40% higher than that of the other two methods. The specific surface area of the adsorbent synthesized via the SG technique (23 m²/g) was almost double that of the adsorbent prepared by the HT method (12 m²/g) and three times that of the one prepared by the PR method (7 m²/g). The presence of plentiful acid sites from the SG method facilitated the physisorption of Hg⁰, making more Hg⁰ available to be oxidized to HgO by the redox sites and thus giving the adsorbent prepared by the SG method the highest Hg⁰ removal efficiency. The strong oxidative ability accelerated the oxidation of the physically adsorbed Hg⁰ to HgO, which explained the higher Hg⁰ removal efficiency of the sample prepared using the HT method than that of the one synthesized by the PR technique. During the whole Hg⁰ removal cycles, chemisorption dominated, with the initial adsorption stage and the external mass-transfer process playing important roles.

Key words: Synthesis methods; Hg⁰ capture; MnO_x; Acidity; Oxidative ability

1 Introduction

Mercury poses a great threat to the environment and human health owing to its high toxicity and long residence (Liu H et al., 2020; Ye et al., 2022d). The consumption of fossil fuels accounts for ca. 35% of the totally produced mercury and around 25% of the global emissions come from anthropogenic sources in China (Xu et al., 2015). Faced with such a severe environmental problem, a national standard GB13223-2011 (MEP, 2011) was issued to illustrate the emission limit of mercury and the Chinese government also approved the “Minimata convention” in 2013, demonstrating that great efforts should be made to effectively reduce the emission of mercury (Wang Z et al., 2020).

In coal-fired flue gas, the emitted mercury can be classified into three categories, namely elemental mercury (Hg⁰), oxidized mercury (Hg²⁺), and particulate-bounded mercury (Hg^p) (Ye et al., 2022b). These last two species can be easily captured by existing air pollution control devices because of the satisfactory solubility of Hg²⁺ and the strong adhesion of Hg^p to the fly ash surfaces, whereas its insolubility and high volatility make Hg⁰ hard to remove. Thus, improving Hg⁰ removal performance is recognized as the key step in reducing mercury emissions (Ye et al., 2021).

To date, adsorption has been shown to be an effective and mature technology to remove Hg⁰ from the flue gas (Chalkidis et al., 2019a). The performance of the adsorbents, the key component in this technique, always dictates the Hg⁰ removal efficiency of the whole system. Several adsorbents, including carbon- and zeolite-based systems, do have satisfactory Hg⁰ capture capability in a certain temperature window (Liu DJ et al., 2020b; Liu H et al., 2020). As a typical transition metal oxide, MnO_x has been proven to be suitable for Hg⁰ removal due to the merits of its acidity, its plentiful surface oxygen vacancies, and its

✉ Dong YE, Richard32@126.com
Haining WANG, whnfyy@163.com

ORCID Dong YE, <https://orcid.org/0000-0001-8299-224X>
Haining WANG, <https://orcid.org/0000-0003-4653-0819>

Received July 14, 2022; Revision accepted Aug. 18, 2022;
Crosschecked Dec. 6, 2022

© Zhejiang University Press 2023

superior oxygen migration ability (Yang et al., 2019). Prepared MnO_x nanotubes, nanorods, and nanowires can effectively capture Hg^0 from simulated flue gas (Chalkidis et al., 2019b).

It is acknowledged that apart from the formula, the preparation method also significantly affects the activity of the adsorbent material (Ye et al., 2022a). It is reported that precipitation (PR), hydrothermal (HT), and sol-gel (SG) methods are recognized as the most commonly used techniques for its preparation (Gao et al., 2010; Liu et al., 2013). Each of the methods has its own merits and drawbacks. However, there has been no systematic analysis and comparison of the impacts of the synthesis conditions on the physico-chemical properties and Hg^0 removal activity of MnO_x , and it is those which will be extensively explored in this study. By this means, structure–performance relationships of the adsorbents can be established, and through exploring the detailed Hg^0 capture pathways, the active sites and the key factors involved in the Hg^0 removal cycles can be revealed. Knowledge of such effects can help to increase adsorbent Hg^0 capture capability to its maximum extent and lay a solid foundation for the effective reduction of mercury emission and the practical application of the adsorbents.

2 Experimental

2.1 Preparation of the adsorbents

MnO_x prepared using the SG method (denoted as Mn-SG): $\text{Mn}(\text{NO}_3)_2$ and citric acid with the molar ratio of 1/2 were dissolved in 30-mL deionized water. After stirring for 3 h, a beaker of transparent sol was obtained and then placed in an oven at 80 °C. Until the foam-like product was formed, the powder was dried in an oven (DHG-9256a, Shanghai Zollo Instrument Co., Ltd., China) at 110 °C for 8 h and finally calcined in a muffle furnace (SGM·M8/10, Guangzhou Hangxin Scientific Instrument Co., Ltd., China) at 500 °C for 5 h.

MnO_x synthesized via the PR method (denoted as Mn-PR): Certain amount of $\text{Mn}(\text{NO}_3)_2$ was dissolved in 30-mL H_2O , which was then slowly added into the excess ammonia solution under vigorous stirring. After 3 h, the produced paste was separated by centrifuge (TG20-WS, Shanghai Chuan Hong Yiqi Co., Ltd., China) and then washed with H_2O . After drying at

110 °C in an oven (DHG-9256a, Shanghai Zollo Instrument Co., Ltd., China) for 8 h, the product was calcined in a muffle furnace (SGM·M8/10, Guangzhou Hangxin Scientific Instrument Co., Ltd., China) at 500 °C for 5 h.

MnO_x prepared using the HT method (denoted as Mn-HT): The calculated amount of $\text{Mn}(\text{NO}_3)_2$ was dissolved in 30-mL deionized water, which was then dropwise added into 40-mL 5-mol/L NaOH solution. After stirring for 3 h, the mixture was transferred to a 100-mL Teflon autoclave. The HT process at 120 °C in an oven (DHG-9256a, Shanghai Zollo Instrument Co., Ltd., China) lasted for 16 h. Then the brownish paste was washed six times, followed by drying in an oven (DHG-9256a, Shanghai Zollo Instrument Co., Ltd., China) at 110 °C for 8 h. Finally, the powder was calcined in a muffle furnace (SGM·M8/10, Guangzhou Hangxin Scientific Instrument Co., Ltd., China) at 500 °C for 5 h.

2.2 Reaction systems

The Hg^0 capture capability of the serial samples was evaluated in a fixed-bed micro-reactor (PXJF-6-2A, Tianjin Golden Eagle Technology Co., Ltd., China). In each 7.5-h test, a 0.1-g sample was used. The simulated flue gas consisted of 5% O_2 , 200- $\mu\text{g}/\text{m}^3$ Hg^0 , and N_2 in balance. The total flow rate was 600 mL/min, corresponding to a gas hourly space velocity of 360 L/(g·h). Hg^0 vapour was generated through a mercury permeation tube (QMG-6-6) placed in a U-shaped quartz tube. The temperature of the water bath was maintained at 32 °C. The inlet and outlet Hg^0 concentrations were recorded using an online mercury analyzer (RA-915M, LUMEX Ltd., Russia). Adsorbent Hg^0 removal efficiency (η) was determined using the following equation:

$$\eta = 100\% \times \frac{\text{Hg}_{\text{in}}^0 - \text{Hg}_{\text{out}}^0}{\text{Hg}_{\text{in}}^0}, \quad (1)$$

where Hg_{in}^0 ($\mu\text{g}/\text{m}^3$) and Hg_{out}^0 ($\mu\text{g}/\text{m}^3$) are ascribed to the inlet and outlet concentrations of Hg^0 , respectively.

2.3 Characterizations

X-ray diffraction (XRD) data in the scanning range of 10°–90° were collected on Rigaku apparatus (Rigaku, D/max-2200, Japan) using the radiation source of Cu K α . Transmission electron microscope

(TEM) images were acquired on FEI Tecnai F20 (FEI, USA), which clearly showed the morphology of the investigated samples.

N_2 adsorption experiments were conducted on Quantachrome Autosorb-1 apparatus. Adsorbent specific surface area and pore size distribution were determined based on N_2 adsorption-desorption isotherms using the Brunauer-Emmett-Teller (BET) equation and the Barrett-Joyner-Halenda (BJH) method, respectively. The degas temperature was set at 300 °C.

H_2 -temperature programmed reduction (H_2 -TPR) profiles were obtained on Micromeritics apparatus (ChemiSorb 2720 TPx, Micromeritics, USA). A sample of 100 mg was held at 300 °C in Ar for 1 h and then cooled to 50 °C. Under 5% H_2 /Ar atmosphere, the sample was finally heated to 800 °C with a ramping rate of 10 °C/min. H_2 consumption was analyzed using a thermal conductivity detector (TCD).

NH_3 -temperature programmed desorption (NH_3 -TPD) profiles were recorded on Micromeritics apparatus (ChemiSorb 2720 TPx, Micromeritics, USA). Briefly, 0.1 g sample was held at 300 °C in Ar for 1 h, followed by lowering the temperature to 50 °C. Given saturation with NH_3 and purging by N_2 , the sample was finally heated to 800 °C in N_2 . The outlet NH_3 signal was analyzed using the TCD.

X-ray photoelectron spectroscopy (XPS) analysis was conducted on an ESCALab220i-XL electron spectrometer. All the binding energies were calibrated with a definite C 1s line of 284.6 eV. Raman spectra of the investigated samples were recorded by micro-Raman spectroscopy (Renisaw, InVia).

Hg^0 temperature-programmed desorption (Hg^0 -TPD) was carried out in a fixed-bed micro-reactor (PXJF-6-2A, Tianjin Golden Eagle Technology Co., Ltd., China). As with the procedures of the NH_3 -TPD characterization, the desorption starts from 150 to 450 °C in N_2 as the pretreatment, Hg^0 saturation, and N_2 purging stages end. The outlet signal of Hg^0 was collected using an online mercury analyzer (RA-915M, LUMEX Ltd., Russia).

3 Results and discussion

3.1 Performance of the adsorbents

The Hg^0 capture capabilities of the serial adsorbents are illustrated in Fig. 1. Among these three

samples, the Mn-SG method exhibits the highest activity, followed by Mn-HT and Mn-PR. At 150 °C, ca. 90% Hg^0 removal efficiency is achieved by Mn-SG, ca. 40% higher than that of the other two samples. As the temperature rises, a downward trend in the Hg^0 removal efficiency is observed for Mn-SG and Mn-PR. By contrast, Mn-HT presents a volcano-shaped activity profile with adsorbent Hg^0 removal efficiency reaching a peak value of ca. 60% at 200 °C. This result indicates that there must exist some variation in the physico-chemical properties of these three samples, which brings about different adsorbent Hg^0 abatement activities.

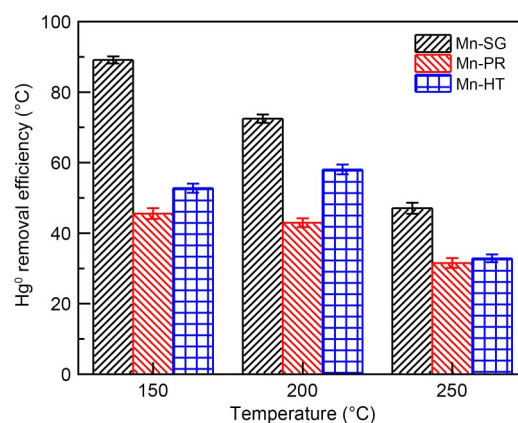


Fig. 1 Hg^0 capture capability of the serial adsorbents

3.2 Textural structures of the adsorbents

The micro morphology of these three investigated adsorbents is illustrated in Fig. 2. It can be seen that all the samples present a morphology of irregular particles fused together, suggesting that morphology is not the main explanation for the variations in the Hg^0 capture capability of the adsorbents. Table 1 summarizes the N_2 adsorption results of the samples. It is observed that the specific surface area of the Mn-SG adsorbent is almost double that of the Mn-HT adsorbent and three times that of the precipitation one. This demonstrates that an increased number of surface-active sites were available for Hg^0 capture and contributed to the elevated Hg^0 removal performance of Mn-SG.

XRD patterns are shown in Fig. 3a, and can be used to express the crystal information from the samples. In both the Mn-PR and Mn-HT samples, the peaks are those of Mn_2O_3 , whereas the bands indexed to Mn_3O_4 crystallites are present only for Mn-SG. Moreover, a decrease in the peak intensity occurs for Mn-SG. This result demonstrates that the growth of

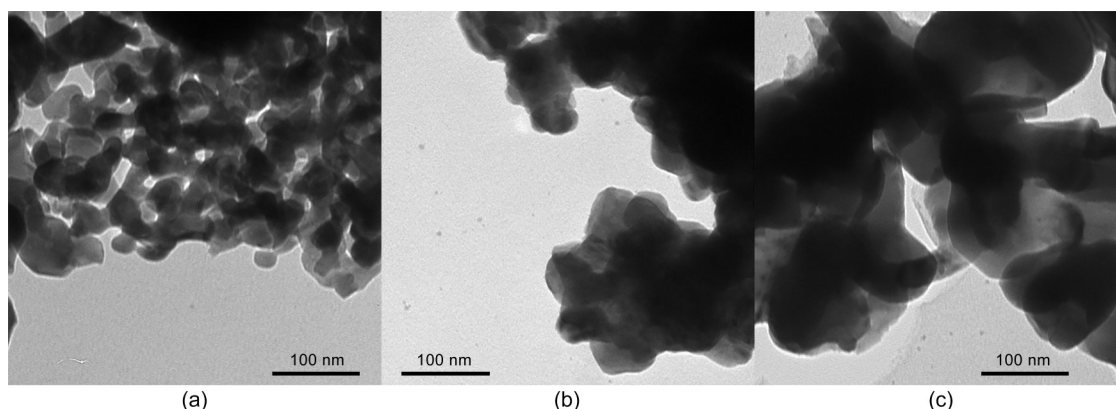


Fig. 2 TEM images of Mn-SG (a), Mn-PR (b), and Mn-HT (c)

Table 1 N₂ adsorption results of the adsorbents

Sample	Surface area (m ² /g)	Pore size (nm)	Pore volume (cm ³ /g)
Mn-SG	23	26.8	0.164
Mn-PR	7	25.5	0.046
Mn-HT	12	27.3	0.087

the crystals is suppressed and a relatively high specific surface area is in turn obtained, as is evidenced by the N₂ adsorption results in Table 1. The local structures of these three samples are further explored through Raman spectroscopy and the related spectra are shown in Fig. 3b. It can be seen that all the samples exhibit three peaks in the wavenumber range of 200–900 cm⁻¹. Peaks at ca. 308, 354, and 643 cm⁻¹ correspond to the out-of-plane bending modes of MnO_x, asymmetric stretch of bridge oxygen species (Mn-O-Mn), and symmetric stretch of MnO_x groups, respectively (Ramesh et al., 2008).

3.3 Chemical properties of the adsorbents

The NH₃-TPD method was employed to study the acidity of the serial adsorbents and the NH₃ adsorption quantity can be used to elucidate the number of surface acid sites. As is illustrated in Fig. 4, Mn-SG possesses the largest number of surface acid sites, followed by Mn-PR and Mn-HT. That would contribute to the physisorption of Hg⁰ and partially explains the highest Hg⁰ removal efficiency of Mn-SG among these three samples. It also indicates that, after acidity, some other properties, such as oxidative ability, play a part in the Hg⁰ capture capability of the adsorbents.

H₂-TPR profiles of the samples are presented in Fig. 5a and demonstrate their redox properties. As

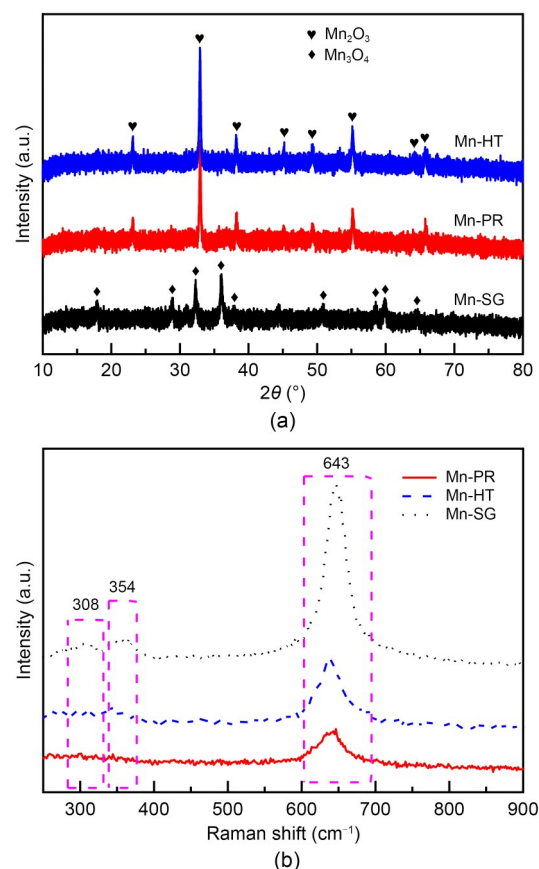


Fig. 3 XRD patterns (a) and Raman spectra (b) of the adsorbents

reported in the literature, the peak centered at ca. 320 °C can be ascribed to the transformation of MnO₂ to Mn₂O₃, whereas the reduction of Mn₂O₃ to Mn₃O₄ explains the presence of the peak at ca. 395 °C; the formation of MnO gives rise to the band located in the higher temperature region (Yang et al., 2015; Jia et al., 2016; Liu et al., 2018). By calculating the integrated

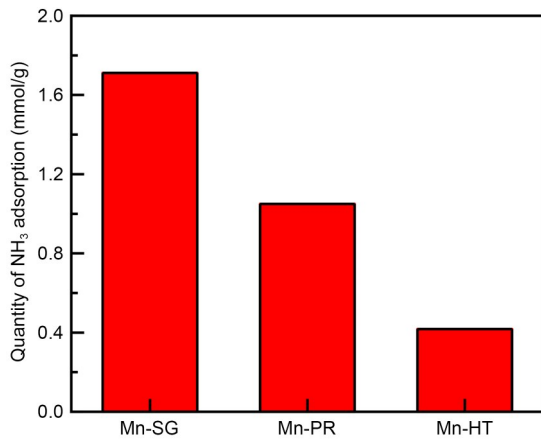


Fig. 4 NH₃-TPD results of the adsorbents

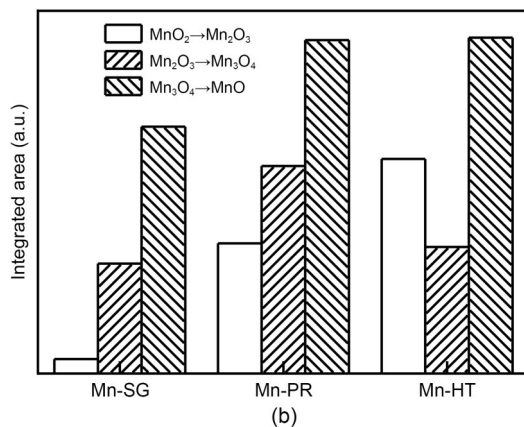
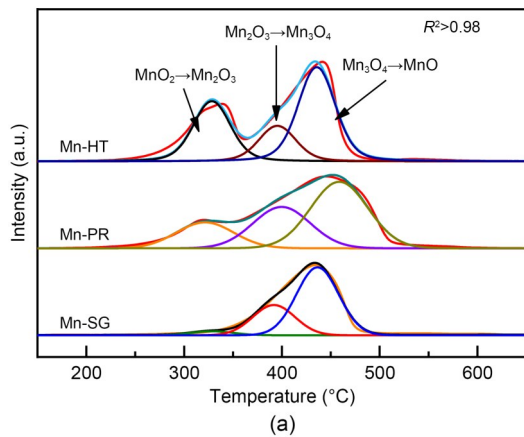


Fig. 5 H₂-TPR profiles (a) and semi-quantitative calculation results (b) of the adsorbents

areas of these three peaks, it seems that Mn-HT possesses the largest proportion of Mn⁴⁺, followed by Mn-PR and Mn-SG. Thus, Mn-HT exhibits an enhanced oxidative ability compared with the other two samples, which can explain its higher Hg⁰ removal efficiency compared with that of Mn-PR. However, the superior

Hg⁰ capture capability of Mn-SG demonstrates that oxidizability is not the unique factor for deciding the performance of an adsorbent and that acidity must also be a factor and will play a role.

The XPS technique was selected to study the adsorbent surface atom environment. Mn 2p spectra of the serial samples are shown in Fig. 6a. Through curve-fitting, the sub-peaks centered at ca. 646, 642, and 640 eV can be attributed to Mn⁴⁺, Mn³⁺, and Mn²⁺, respectively (Yang et al., 2011b). After calculation, it can be seen that Mn⁴⁺ are the most plentiful on the Mn-HT surface, followed by Mn-PR and Mn-SG (Table 2). Fig. 6b illustrates the adsorbent O 1s spectra. As reported in the literature, the sub-peak ranging

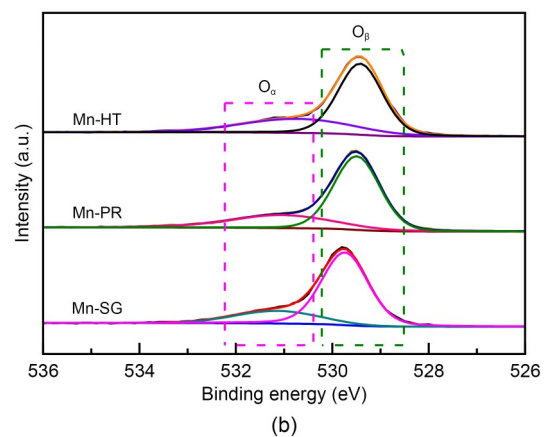
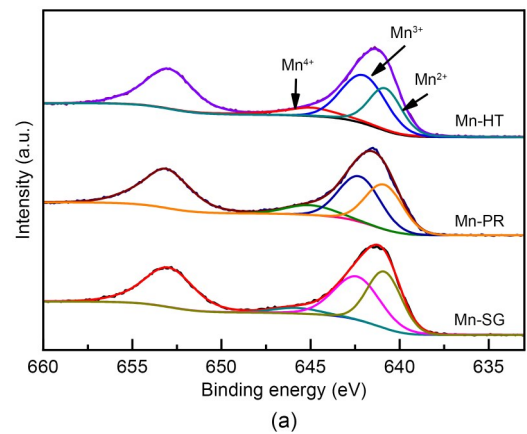


Fig. 6 XPS spectra: (a) Mn 2p; (b) O 1s

Table 2 XPS data of the adsorbents

Sample	Relative content (%)			
	Mn ⁴⁺	Mn ³⁺	Mn ²⁺	O _α
Mn-SG	6.0	49.0	45.0	22.1
Mn-PR	11.8	46.6	41.5	29.3
Mn-HT	15.2	50.0	34.7	32.2

between 530 and 531 eV is related to chemisorbed oxygen (O_a), including O_2^- , O_2^{2-} , and OH^- , whereas the band located at 529–530 eV is indexed to lattice oxygen (O_b) (Qu et al., 2013). The relative concentration of O_a was calculated in Table 2 and follows the order of Mn-HT>Mn-PR>Mn-SG, which is indicative of a strong oxidative ability of Mn-HT and supports the conclusions drawn from the H_2 -TPR results in Fig. 5.

3.4 Hg^0 removal mechanisms

Among these three investigated samples, it can be seen that Mn-SG exhibits the best Hg^0 removal performance between 150 and 250 °C. It is thus reasonable to select this sample for the investigation of the Hg^0 adsorption mechanisms, results of which can help discovery of the important factors during the Hg^0 removal cycles and thus the development of new adsorbents with superior Hg^0 capture capabilities.

As an important step during Hg^0 capture, the mass-transfer process affects the adsorbent Hg^0 removal efficiency to a considerable extent. According to the literature, the mass transfer process mainly consists of an external mass transfer, a global mass transfer, and an internal mass transfer, which can be expressed by the following four equations (Fulazzaky et al., 2013):

$$\ln\left(\frac{C_0}{C_s}\right) = [k_L a]_f \times t, \quad (2)$$

$$[k_L a]_f = [k_L a]_g \times e^{-b \ln(q_t)}, \quad (3)$$

$$[k_L a]_d = [k_L a]_g - [k_L a]_f, \quad (4)$$

$$\ln(q_t) = B + \frac{1}{b} \times \ln(t), \quad (5)$$

where C_0 is the inlet concentration of Hg^0 ($\mu g/m^3$), C_s is the outlet concentration of Hg^0 ($\mu g/m^3$), t is the Hg^0 capture accumulation time, a is the surface of interfacial liquid-solid (m^{-1}), b is the adsorbate-adsorbent affinity parameter ($g \cdot h/mg$), q_t is the Hg^0 cumulative quantity (mg/g), B is the potential mass transfer index corresponding to the driving force of mass transfer (mg/g), k_L is the mass transfer coefficient (m/h), $[k_L a]_f$ is the external mass transfer factor (h^{-1}), $[k_L a]_g$ is the global mass transfer factor (h^{-1}), and $[k_L a]_d$ is the internal mass transfer factor (h^{-1}).

Fig. 7a illustrates the linear fitting results of the experimental data. The correlation coefficients (R^2) at 150, 200, and 250 °C were calculated to exceed 0.998

(Table 3). Thus, it is reasonable to use the index B and parameter b to scrutinize the mass transfer potential and adsorbate-adsorbent affinity for Hg^0 capture. Given an ongoing adsorption process, the absolute values of $[k_L a]_f$, $[k_L a]_d$, and $[k_L a]_g$ continuously decrease and almost reach zero after 240 min, suggesting that the mass transfer process mainly influences the initial Hg^0 adsorption stage and that, after a period of time, its impact can be neglected. Considering that Hg^0 is a basic molecule, the physically adsorbed Hg^0 in the initial Hg^0 capture stage would occupy parts of the adsorbent surface acid sites (Zhao et al., 2020). That is to say, the accumulation of Hg^0 would lead to a decreased surface acidity and thus create a repulsion force between the adsorbate and the adsorbent. As a result, a negative value of $[k_L a]_d$ is obtained.

The adsorption kinetics of Hg^0 over the adsorbents were explained through the fitting of four models, namely the pseudo-first-order (Eq. (6)), the pseudo-second-order (Eq. (7)), the Webber-Morris (Eq. (8)), and the Elovich (Eq. (9)) models, to the experimental data (Chen et al., 2015). Among them, both the pseudo-second-order model and the Elovich model explain the chemisorption process, while the external mass transfer process and the internal mass transfer process can be expressed by the pseudo-first-order model and the Webber-Morris model (Yang et al., 2021). In addition, the Elovich model can also illustrate the initial Hg^0 adsorption stage.

$$\frac{dq_t}{dt} = k_1(q_e - q_t), \quad (6)$$

$$\frac{dq_t}{dt} = k_2(q_e - q_t)^2, \quad (7)$$

$$q_t = k_p t^{1/2} + c, \quad (8)$$

$$q_t = \frac{1}{\beta} \ln(t + \alpha\beta) - \frac{1}{\beta} \ln\left(\frac{1}{\alpha\beta}\right), \quad (9)$$

where k_1 , k_2 , q_e , k_p , c , α , and β are attributed to the pseudo-first-order rate constant (min^{-1}), the pseudo-second-order rate constant ($\mu g/(g \cdot min)$), the adsorbent equilibrium adsorption capacity ($\mu g/g$), the intraparticle diffusion coefficient ($\mu g/(g \cdot min^{1/2})$), the constant related to the boundary conditions ($\mu g/g$), the initial adsorption rate constant ($\mu g/(g \cdot min^{1/2})$), and the desorption rate constant ($g/\mu g$), respectively.

As presented in Fig. 8 and Table 4, the pseudo-first-order, the pseudo-second-order, and the Elovich models can describe the Hg^0 capture process on

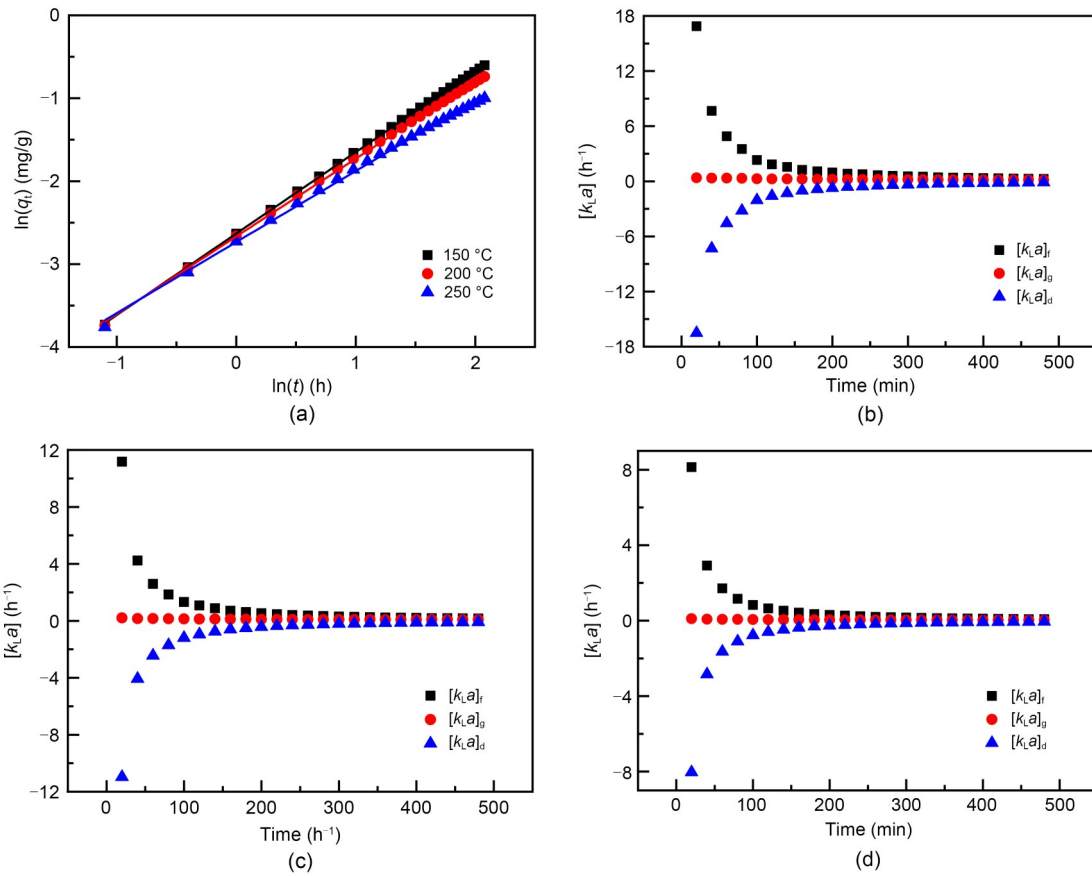


Fig. 7 Linear regression analysis (a) and curves of $[k_1a]_g$, $[k_1a]_d$, and $[k_1a]_s$ versus time at 150 °C (b), 200 °C (c), and 250 °C (d)

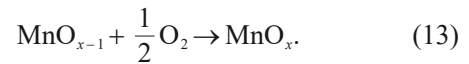
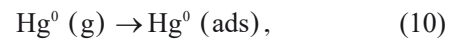
Table 3 Linear regression results

Temperature (°C)	B (mg/g)	b (g·h/mg)	R^2
150	1.017	-2.632	0.99989
200	1.066	-2.667	0.99955
250	1.167	-2.734	0.99805

Mn-SG effectively. As reported in the literature, the initial adsorption stage and the external mass transfer process play important roles, and that, to some extent, supports the conclusions drawn from Fig. 7 (Shi et al., 2016; Liu DJ et al., 2020a).

XPS was conducted to investigate the variations in the valence state of the adsorbent surface atoms after the adsorption of Hg^0 , to help elucidate the possible Hg^0 capture mechanisms. According to Fig. 9 and Table 5, the decrease in the relative contents of Mn^{4+} , Mn^{3+} , and O_a indicates that these species function as the active sites to directly participate in the removal of Hg^0 . The photoelectron peaks centered at ca. 101 and 105 eV in Fig. 9c and the Hg^0 -TPD profile in Fig. 9d demonstrate that the adsorbed mercury species are

present in the form of HgO (Yang et al., 2011a). Thus, the Hg^0 capture pathways over Mn-SG can be summarized as follows (Eqs. (10)–(13) and Fig. 10) (Wang HN et al., 2020):



3.5 Discussion

Based on our previous study, the capture of Hg^0 can be considered as a dual-site reaction: adsorbent surface acid sites are primarily responsible for the physisorption of Hg^0 , whereas the redox sites participate in the oxidation of the physically adsorbed Hg^0 to HgO (Ye et al., 2022a, 2022c). In the case of Mn-SG, abundant surface acid sites are available to physically adsorb Hg^0 , which provides sufficient reactant for the next oxidation step and hence enables a large portion

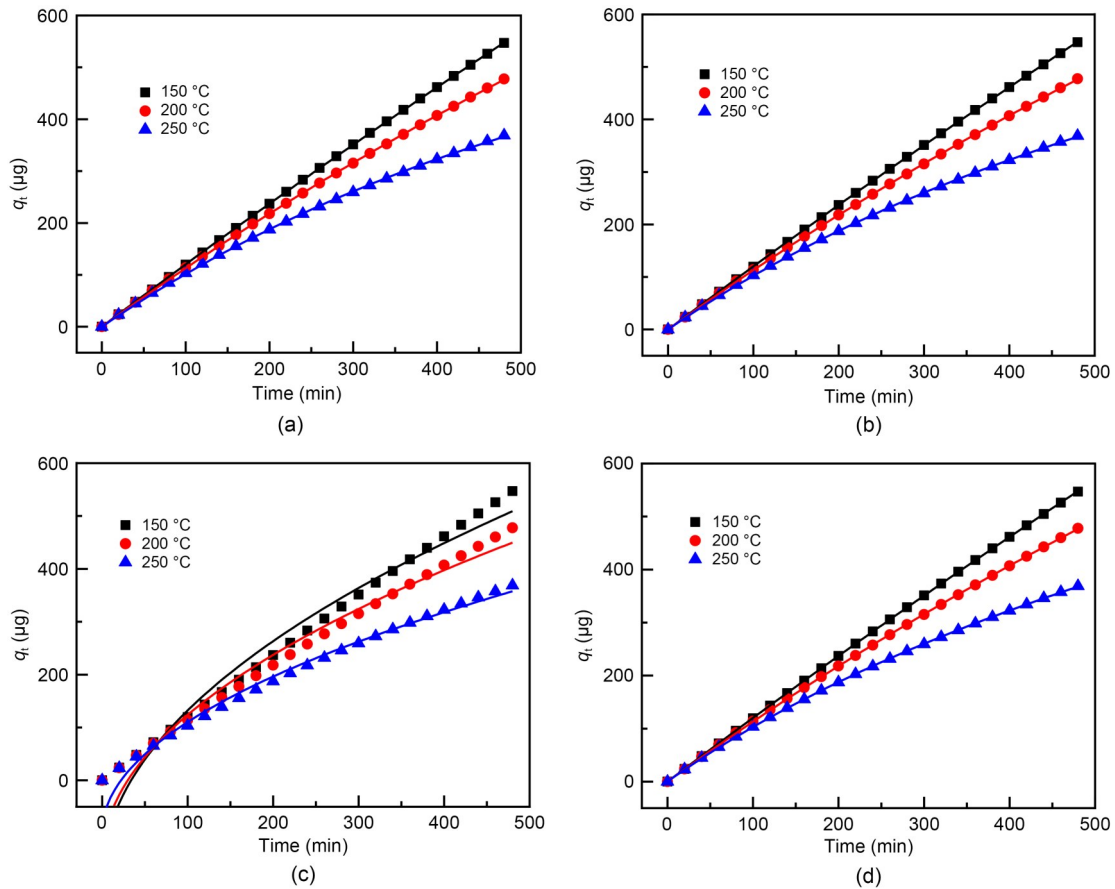


Fig. 8 Curve fitting of the experimental data by the pseudo-first-order (a), pseudo-second-order (b), Weber-Morris (c), and Elovich (d) models

Table 4 Correlation coefficients (R^2) of the pseudo-first-order, pseudo-second-order, Weber-Morris, and Elovich models

Temperature (°C)	Correlation coefficient, R^2			
	Pseudo-first-order	Pseudo-second-order	Weber-Morris	Elovich
150	0.99999	0.99999	0.97470	0.99999
200	0.99997	0.99998	0.98114	0.99999
250	0.99981	0.99991	0.99210	0.99997

of the Hg^0 to be efficiently oxidized to HgO by the sites with oxidative ability. Only a small part of the gaseous Hg^0 is free from capture by the adsorbent and thus a relatively high Hg^0 removal efficiency is observed. While for the other two samples, even though an enhanced oxidative ability is obtained, yet the relative low amount of surface acid sites interferes with the physisorption of Hg^0 . Therefore, only a limited amount of Hg^0 can be involved in the following reaction step and most Hg^0 just passes directly through the adsorbent bed (Ye et al., 2022a). That is to say, that on this occasion, redox sites on Mn-HT and Mn-PR might be superfluous for the oxidation of Hg^0 and the lack

of acid sites constitutes the main barrier to high Hg^0 removal efficiency. Opposite reasons can be used to explain the better Hg^0 capture capability of Mn-HT than that of Mn-PR. Besides, the optimized textural structures are somehow responsible for promoting diffusion of the reactant, which also partially explains the Hg^0 abatement performance order of Mn-SG>Mn-HT>Mn-PR (Chen et al., 2014; Ye et al., 2022c).

As the temperature rises, the differences between the positive effect of the enhanced Hg^0 oxidation step and the inhibitory impact of the weakened Hg^0 physisorption process mainly determine the trend of the adsorbent Hg^0 capture capability (Ye et al., 2022b). In

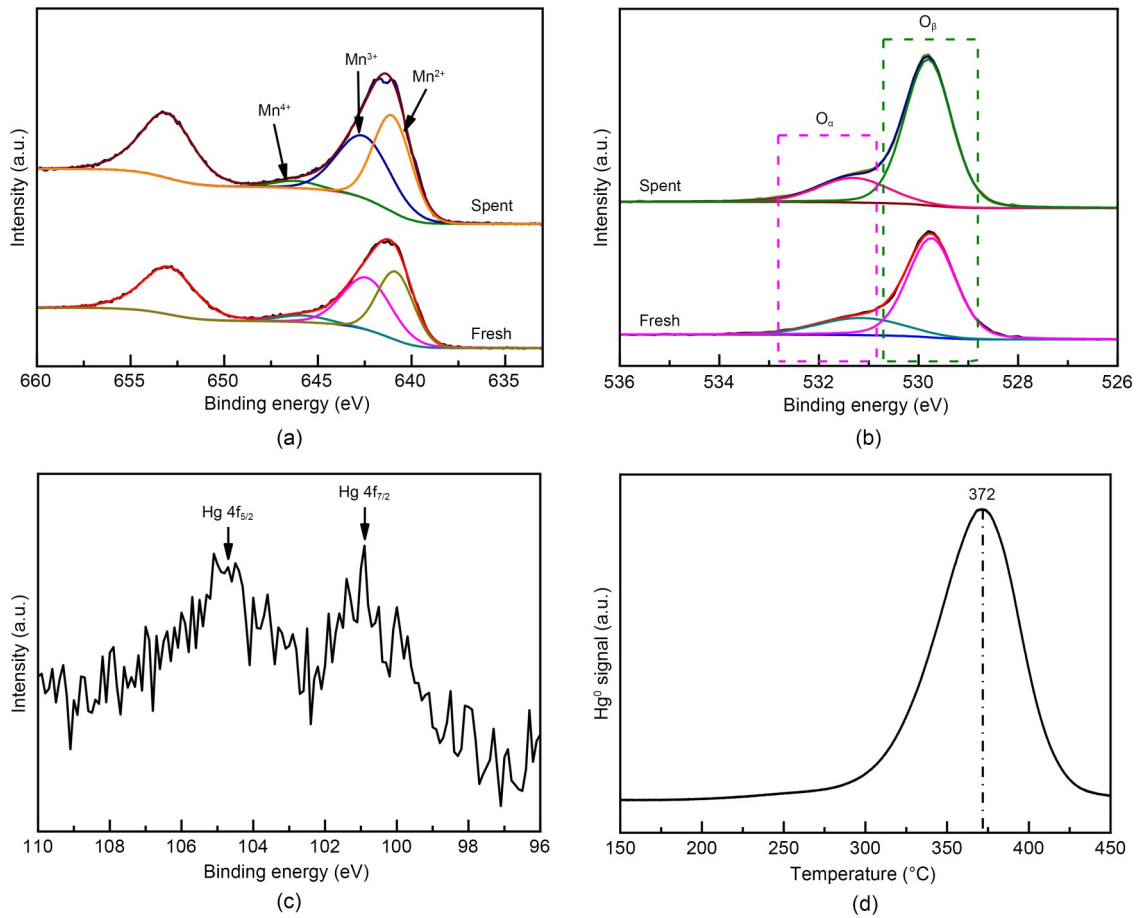


Fig. 9 XPS spectra of the fresh and spent samples: (a) Mn 2p; (b) O 1s; (c) Hg 4f; (d) Hg⁰-TPD profile

Table 5 XPS data of the fresh and spent samples

Sample	Relative content (%)							
	Mn ⁴⁺	Mn ³⁺	Mn ²⁺	O _a	Mn	O	C	Hg
Fresh	6.0	49.0	45.0	22.1	29.0	49.9	21.1	—
Spent	4.2	46.3	49.5	20.0	29.8	50.5	19.5	0.2

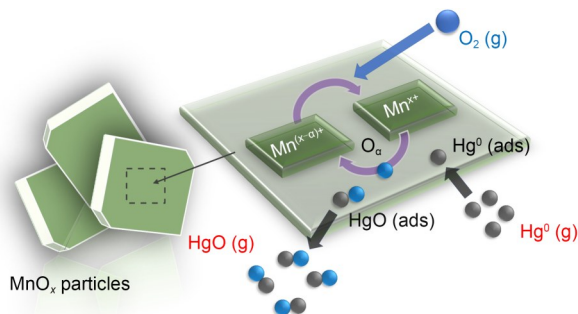


Fig. 10 Hg⁰ removal mechanism over Mn-SG

other words, provided that the promotional impact of the accelerated Hg⁰ oxidation stage is dominant during heating, adsorbent Hg⁰ removal efficiency will be

in turn elevated and vice versa. In the case of Mn-SG and Mn-PR, the suppressed Hg⁰ physisorption process constitutes the main barrier to an increase in the Hg⁰ removal efficiency at higher temperatures and thus there is a downtrend in the adsorbent Hg⁰ capture capability (Yang et al., 2011b, 2011c). By contrast, the positive effect of the facilitated Hg⁰ oxidation stage can overpower the above-mentioned negative impact for Mn-HT, thereby bringing out an elevated Hg⁰ removal efficiency at 200 °C. With a further increase in temperature, this inhibitory effect would dominate and consequently adsorbent Hg⁰ removal efficiency would decline.

In summary, acidity and oxidizability both play a role in the Hg⁰ capture capability of an adsorbent. A satisfactory acidity can ensure sufficient physisorption of Hg⁰ and the sites with a superior oxidative ability will then contribute to the efficient oxidation of the physisorbed Hg⁰ to HgO, and enable Hg⁰ to be effectively removed from the flue gas.

4 Conclusions

In this study, we synthesized MnO_x adsorbents using the SG, PR, and HT methods and tested their Hg^0 removal performance. Some conclusions are drawn below:

(1) Adsorbent prepared using the SG method exhibits the best performance; ca. 90% Hg^0 removal performance is reached at 150 °C, almost doubling compared with that of Mn-PR.

(2) The presence of plentiful acid sites facilitates the physisorption of Hg^0 , providing ample Hg^0 for oxidation to HgO by the redox sites and subsequently enabling Mn-SG with a relatively high Hg^0 removal efficiency.

(3) Chemisorption dominates in all the Hg^0 abatement cycles, in which the initial adsorption stage constitutes the rate-determining step. The Mars-Maessen mechanism can explain the Hg^0 capture pathways over the adsorbents with Mn ions in a high valence state and O_a directly participating in the oxidation of Hg^0 .

Acknowledgments

This work is supported by the Fundamental Research Funds of China Jiliang University and the Zhejiang Provincial Natural Science Foundation of China (No. LQ22E060003).

Author contributions

Yongjin HU and Zhichang JIANG designed the research. Dong YE processed the corresponding data. Dong YE wrote the first draft of the manuscript. Xin LIU helped to organize the manuscript. Haining WANG and Dong YE revised and edited the final version.

Conflict of interest

Dong YE, Yongjin HU, Zhichang JIANG, Xin LIU, and Haining WANG declare that they have no conflict of interest.

Reference

- Chalkidis A, Jampaiah D, Amin MH, et al., 2019a. CeO_2 -decorated α - MnO_2 nanotubes: a highly efficient and regenerable sorbent for elemental mercury removal from natural gas. *Langmuir*, 35(25):8246-8256.
<https://doi.org/10.1021/acs.langmuir.9b00835>
- Chalkidis A, Jampaiah D, Hartley PG, et al., 2019b. Regenerable α - MnO_2 nanotubes for elemental mercury removal from natural gas. *Fuel Processing Technology*, 193:317-327.
<https://doi.org/10.1016/j.fuproc.2019.05.034>
- Chen JH, Cao FF, Chen SZ, et al., 2014. Adsorption kinetics of NO on ordered mesoporous carbon (OMC) and

- cerium-containing OMC (Ce-OMC). *Applied Surface Science*, 317:26-34.
<https://doi.org/10.1016/j.apsusc.2014.08.067>
- Chen JH, Cao FF, Qu RY, et al., 2015. Bimetallic cerium-copper nanoparticles embedded in ordered mesoporous carbons as effective catalysts for the selective catalytic reduction of NO with NH_3 . *Journal of Colloid and Interface Science*, 456:66-75.
<https://doi.org/10.1016/j.jcis.2015.06.001>
- Fulazzaky MA, Khamidun MH, Omar R, 2013. Understanding of mass transfer resistance for the adsorption of solute onto porous material from the modified mass transfer factor models. *Chemical Engineering Journal*, 228:1023-1029
- Gao X, Jiang Y, Fu YC, et al., 2010. Preparation and characterization of $\text{CeO}_2/\text{TiO}_2$ catalysts for selective catalytic reduction of NO with NH_3 . *Catalysis Communications*, 11(5):465-469.
<https://doi.org/10.1016/j.catcom.2009.11.024>
- Jia JB, Zhang PY, Chen L, 2016. The effect of morphology of α - MnO_2 on catalytic decomposition of gaseous ozone. *Catalysis Science & Technology*, 6(15):5841-5847.
<https://doi.org/10.1039/C6CY00301J>
- Liu CX, Chen L, Chang HZ, et al., 2013. Characterization of CeO_2 - WO_3 catalysts prepared by different methods for selective catalytic reduction of NO_x with NH_3 . *Catalysis Communications*, 40:145-148.
<https://doi.org/10.1016/j.catcom.2013.06.017>
- Liu DJ, Zhang Z, Luo F, et al., 2020a. Elemental mercury capture from simulated flue gas by graphite-phase carbon nitride. *Energy & Fuels*, 34(6):6851-6861.
<https://doi.org/10.1021/acs.energyfuels.0c00457>
- Liu DJ, Li CE, Wu J, et al., 2020b. Novel carbon-based sorbents for elemental mercury removal from gas streams: a review. *Chemical Engineering Journal*, 391:123514.
<https://doi.org/10.1016/j.cej.2019.123514>
- Liu H, Chang L, Liu WJ, et al., 2020. Advances in mercury removal from coal-fired flue gas by mineral adsorbents. *Chemical Engineering Journal*, 379:122263.
<https://doi.org/10.1016/j.cej.2019.122263>
- Liu SL, Ji J, Yu Y, et al., 2018. Facile synthesis of amorphous mesoporous manganese oxides for efficient catalytic decomposition of ozone. *Catalysis Science & Technology*, 8(16):4264-4273.
<https://doi.org/10.1039/C8CY01111G>
- MEP (Ministry of Environmental Protection of the People's Republic of China), 2011. Emission Standard of Air Pollutants for Thermal Power Plants, GB13223-2011. National Standards of the People's Republic of China (in Chinese).
- Qu RY, Gao X, Cen KF, et al., 2013. Relationship between structure and performance of a novel cerium-niobium binary oxide catalyst for selective catalytic reduction of NO with NH_3 . *Applied Catalysis B: Environmental*, 142-143:290-297.
<https://doi.org/10.1016/j.apcatb.2013.05.035>
- Ramesh K, Chen LW, Chen FX, et al., 2008. Re-investigating the CO oxidation mechanism over unsupported MnO , Mn_2O_3 and MnO_2 catalysts. *Catalysis Today*, 131(1-4):

- 477-482.
<https://doi.org/10.1016/j.cattod.2007.10.061>
- Shi YJ, Deng S, Wang HM, et al., 2016. Fe and Co modified vanadium-titanium steel slag as sorbents for elemental mercury adsorption. *RSC Advances*, 6(19):15999-16009.
<https://doi.org/10.1039/c5ra26712a>
- Wang HN, Ma W, Yan JB, et al., 2020. Smart modification of HZSM-5 with manganese species for the removal of mercury. *ACS Omega*, 5(30):19277-19284.
<https://doi.org/10.1021/acsomega.0c02877>
- Wang Z, Liu J, Yang YJ, et al., 2020. Insights into the catalytic behavior of LaMnO₃ perovskite for Hg⁰ oxidation by HCl. *Journal of Hazardous Materials*, 383:121156.
<https://doi.org/10.1016/j.jhazmat.2019.121156>
- Xu HM, Xie JK, Ma YP, et al., 2015. The cooperation of Fe-Sn in a MnO_x complex sorbent used for capturing elemental mercury. *Fuel*, 140:803-809.
<https://doi.org/10.1016/j.fuel.2014.10.004>
- Yang LT, Wu J, Li B, et al., 2021. Defective molybdenum disulfide nanosheet for elemental mercury capture in simulated flue gas. *Journal of the Energy Institute*, 94:120-128.
<https://doi.org/10.1016/j.joei.2020.11.007>
- Yang R, Mei CL, Wu XS, et al., 2019. Mn-Cu binary metal oxides with molecular-scale homogeneity for Hg⁰ removal from coal-fired flue gas. *Industrial & Engineering Chemistry Research*, 58(41):19292-19301.
<https://doi.org/10.1021/acs.iecr.9b04005>
- Yang SJ, Guo YF, Yan NQ, et al., 2011a. Capture of gaseous elemental mercury from flue gas using a magnetic and sulfur poisoning resistant sorbent Mn/γ-Fe₂O₃ at lower temperatures. *Journal of Hazardous Materials*, 186(1):508-515.
<https://doi.org/10.1016/j.jhazmat.2010.11.034>
- Yang SJ, Guo YF, Yan NQ, et al., 2011b. Elemental mercury capture from flue gas by magnetic Mn-Fe spinel: effect of chemical heterogeneity. *Industrial & Engineering Chemistry Research*, 50(16):9650-9656.
<https://doi.org/10.1021/ie2009873>
- Yang SJ, Guo YF, Yan NQ, et al., 2011c. Nanosized cation-deficient Fe-Ti spinel: a novel magnetic sorbent for elemental mercury capture from flue gas. *ACS Applied Materials & Interfaces*, 3(2):209-217.
<https://doi.org/10.1021/am100835c>
- Yang Y, Zhang SZ, Wang SW, et al., 2015. Ball milling synthesized MnO_x as highly active catalyst for gaseous POPs removal: significance of mechanochemically induced oxygen vacancies. *Environmental Science & Technology*, 49(7):4473-4480.
- Ye D, Wang XX, Wang RX, et al., 2021. Recent advances in MnO₂-based adsorbents for mercury removal from coal-fired flue gas. *Journal of Environmental Chemical Engineering*, 9(5):105993.
<https://doi.org/10.1016/j.jece.2021.105993>
- Ye D, Wang RX, Wang XX, et al., 2022a. Effects of synthesis methods on the physicochemical properties and Hg⁰ capture capability of MnO₂-CeO₂ mixed oxides. *Applied Surface Science*, 578:151998.
<https://doi.org/10.1016/j.apsusc.2021.151998>
- Ye D, Wang RX, Wang XX, et al., 2022b. Improvement in the Hg⁰ removal performance of CeO₂ by modifying with CuO. *Applied Surface Science*, 579:152200.
<https://doi.org/10.1016/j.apsusc.2021.152200>
- Ye D, Wang XX, Wang RX, et al., 2022c. Relationship between Hg⁰ capture performance and physicochemical properties of CeO₂-CrO_x mixed oxides. *Journal of Environmental Chemical Engineering*, 10(5):108252.
<https://doi.org/10.1016/j.jece.2022.108252>
- Ye D, Wang XX, Wang RX, et al., 2022d. Review of elemental mercury (Hg⁰) removal by CuO-based materials. *Journal of Zhejiang University-SCIENCE A (Applied Physics & Engineering)*, 23(7):505-526.
<https://doi.org/10.1631/jzus.A2100627>
- Zhao HT, Ezeh CI, Yin SF, et al., 2020. MoO₃-adjusted δ-MnO₂ nanosheet for catalytic oxidation of Hg⁰ to Hg²⁺. *Applied Catalysis B: Environmental*, 263:117829.
<https://doi.org/10.1016/j.apcatb.2019.117829>